

## Electronic Supplementary Information

### Efficient photoelectrochemical water oxidation enabled by an amorphous metal oxide-catalyzed graphene/silicon heterojunction photoanode

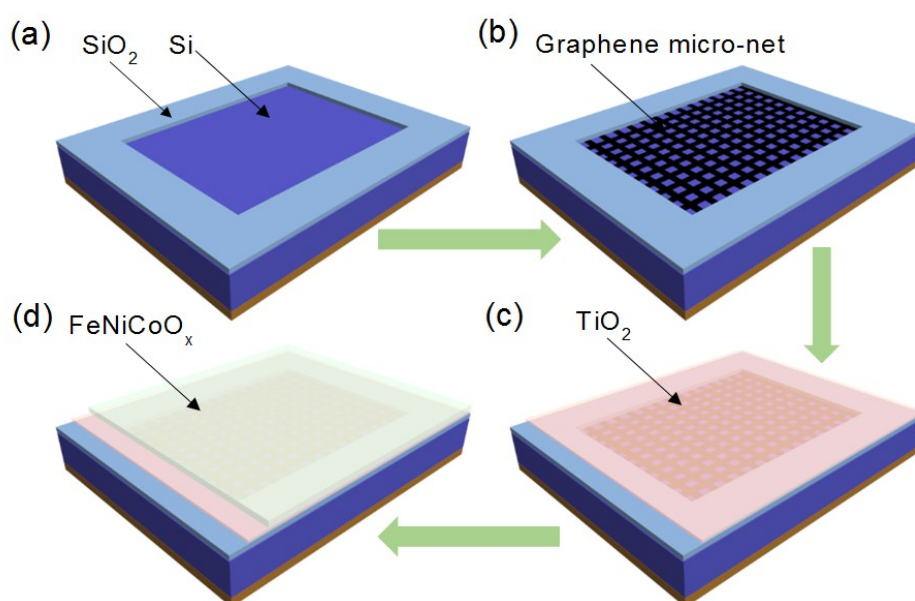
Changli Li,<sup>a</sup> Yequan Xiao,<sup>a</sup> Li Zhang,<sup>a</sup> Yanbo Li,<sup>b</sup> Jean-Jacques Delaunay,<sup>c</sup> Hongwei Zhu<sup>a\*</sup>

<sup>a</sup>State Key Laboratory of New Ceramics and Fine Processing, School of Materials Science and Engineering, Tsinghua University, Beijing 100084, China

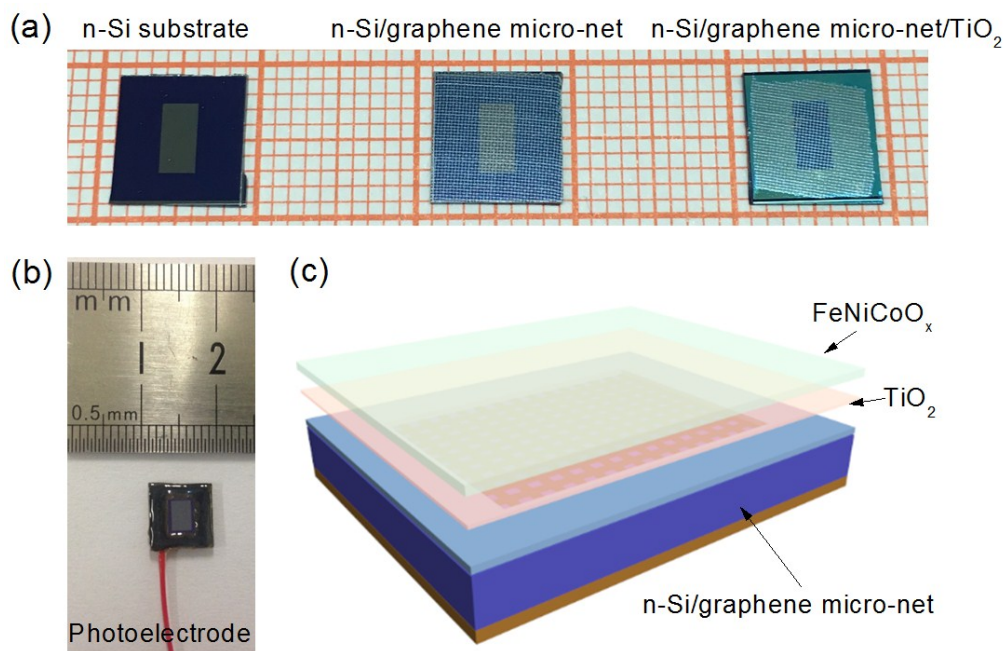
<sup>b</sup>Institute of Fundamental and Frontier Sciences, University of Electronic Science and Technology of China, Chengdu, China

<sup>c</sup>School of Engineering, The University of Tokyo, 7-3-1 Hongo, Bunkyo-ku, Tokyo 113-8656, Japan

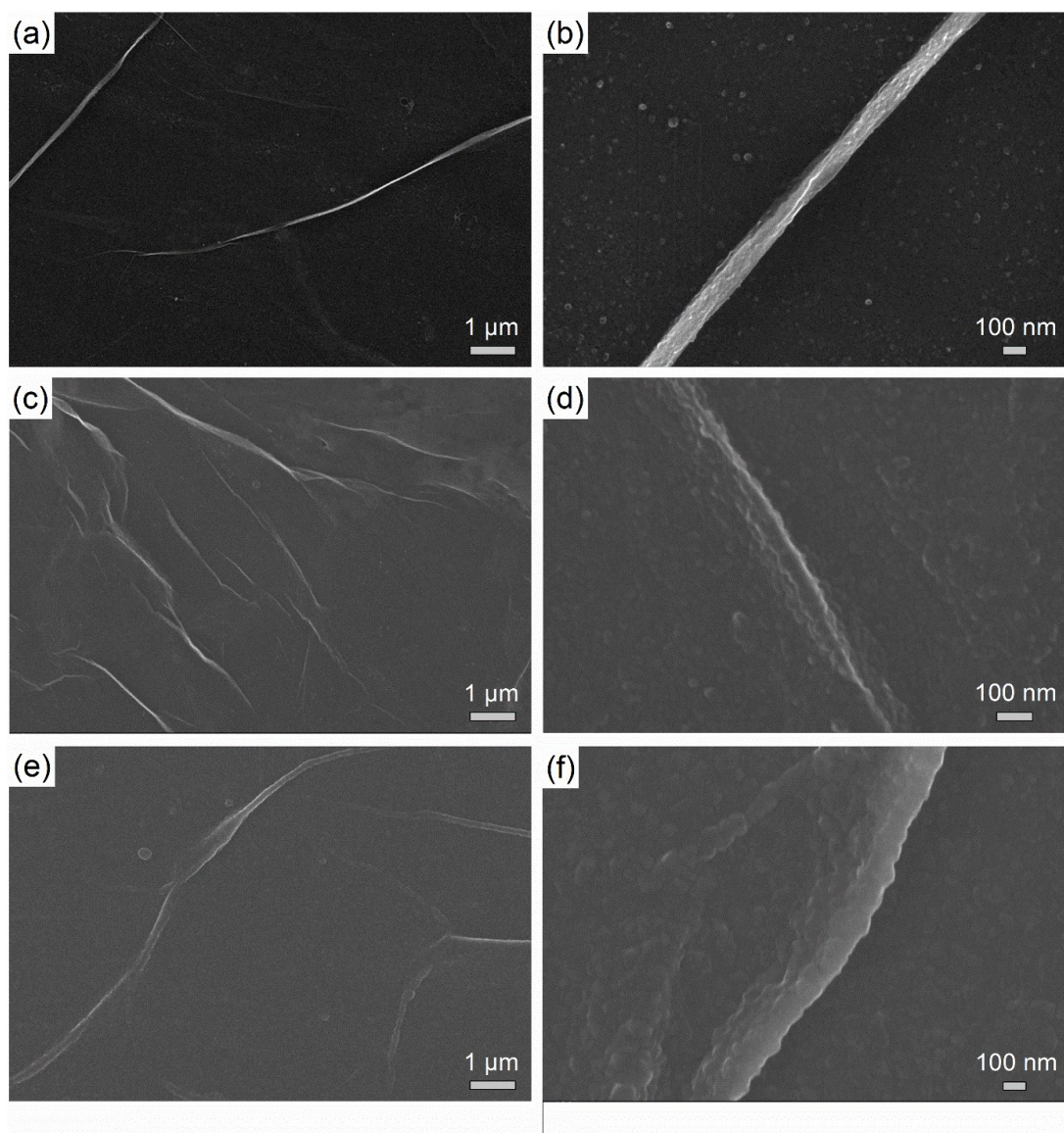
\*Email: hongweizhu@tsinghua.edu.cn



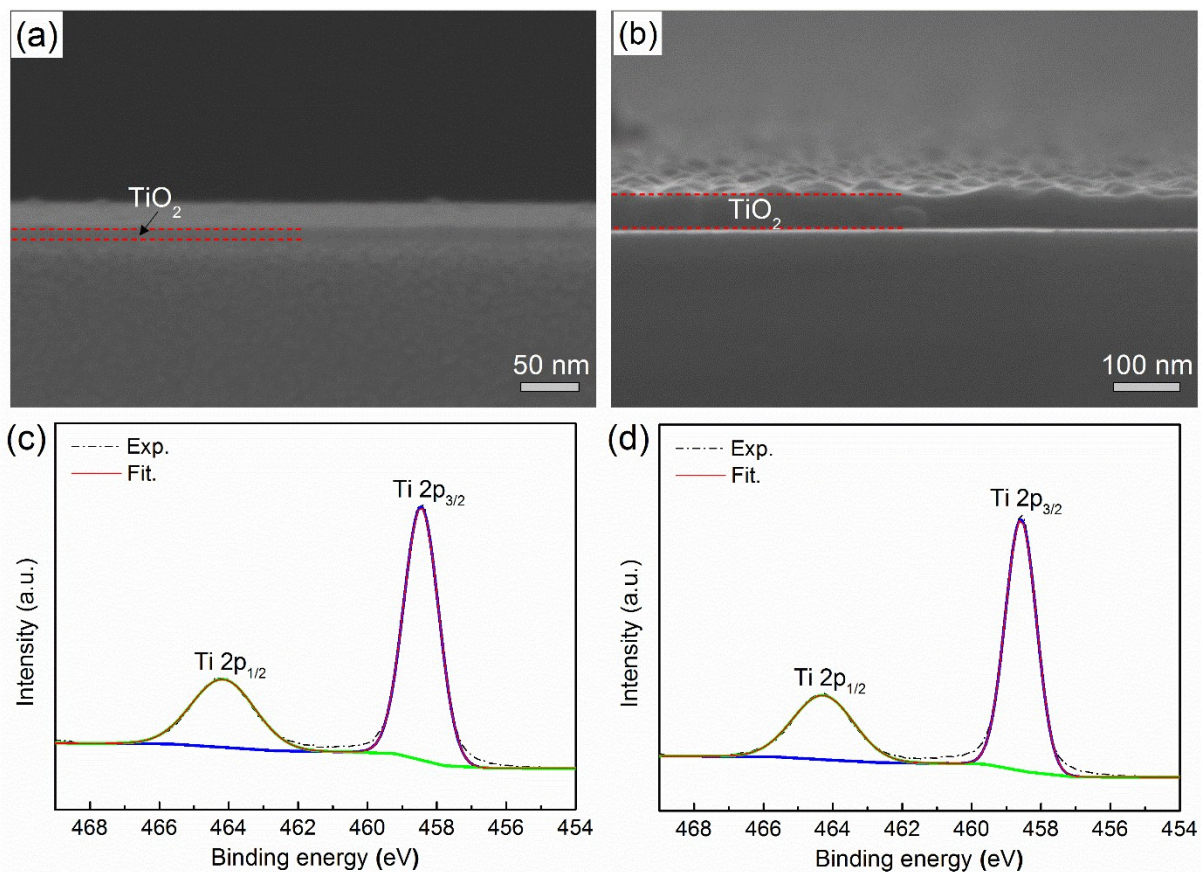
**Figure S1.** Schematic process for the fabrication of Si/graphene/TiO<sub>2</sub>/FeNiCoO<sub>x</sub> photoanode. (a) Si substrate with a 0.1 cm<sup>2</sup> exposed active area prepared by photolithography. (b) Graphene micro-net was transferred onto the Si substrate. (c) TiO<sub>2</sub> thin layer was deposited onto the Si/graphene substrate by ALD. (d) Si/graphene/TiO<sub>2</sub>/FeNiCoO<sub>x</sub> photoanode obtained by deposition of FeNiCoO<sub>x</sub> film by a photochemical method.



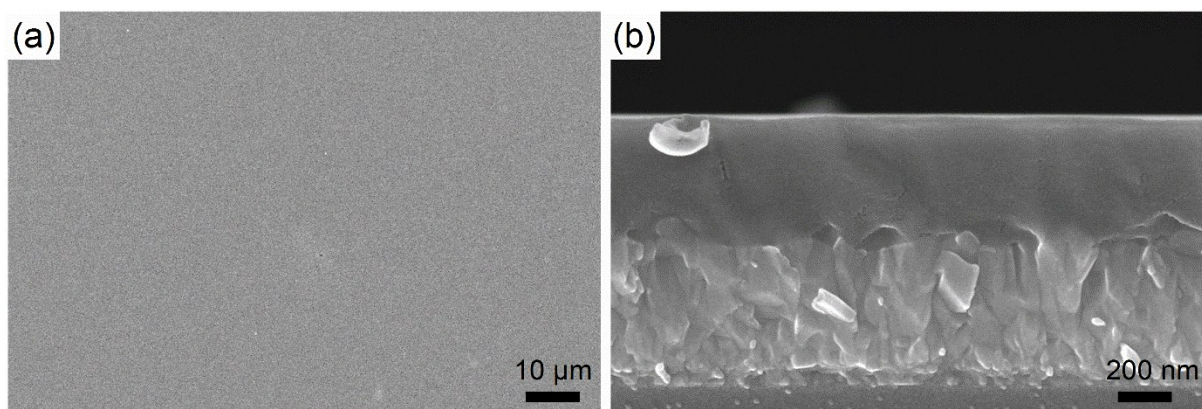
**Figure S2.** (a) Photograph of the Si, Si/graphene and Si/graphene/TiO<sub>2</sub> electrode. (b) Photograph of an encapsulated electrode. (c) Schematic diagram to present the each layer of Si/graphene/TiO<sub>2</sub>/FeNiCoO<sub>x</sub> electrode.



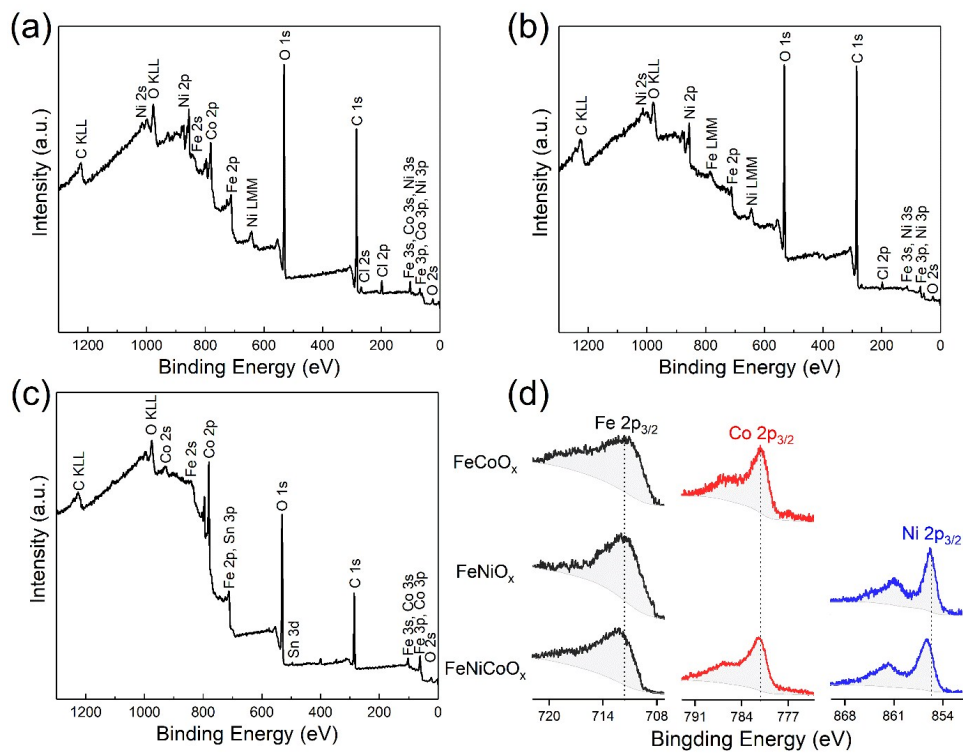
**Figure S3.** FE-SEM images of (a,b) graphene micro-net transferred onto Si substrate, (c,d) Si/graphene/TiO<sub>2</sub> (10 nm) structure, (e,f) Si/graphene/TiO<sub>2</sub> (50 nm) structure.



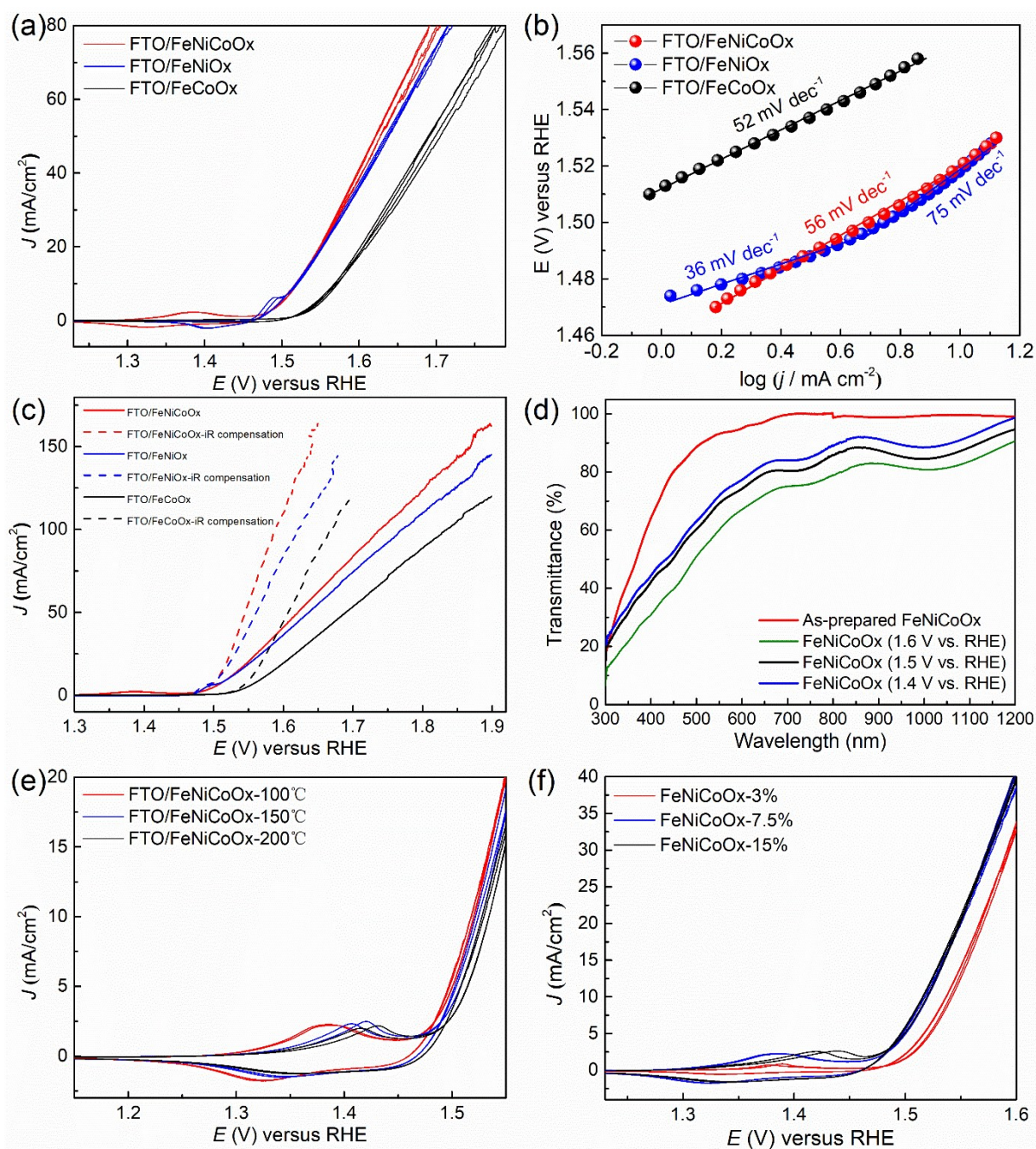
**Figure S4.** Cross-section SEM images of (a) 10 nm- and (b) 50 nm- $\text{TiO}_2$  thin films deposited on n-Si by ALD. XPS spectrum of Ti-2p peaks for the (c) 10 nm- and (d) 50 nm- $\text{TiO}_2$  thin films.



**Figure S5.** (a) Top-view and (b) cross-section SEM images of  $\text{FeNiCoO}_x$  film deposited on FTO substrate.



**Figure S6.** X-ray photoelectron spectroscopy survey scan acquired on FeNiCoO<sub>x</sub> (a), FeNiO<sub>x</sub> (b) and FeCoO<sub>x</sub> (c) on FTO glass. (d) Fe, Co, and Ni 2p<sub>3/2</sub> regions of XPS spectra recorded on the three mixed-metal oxide films.



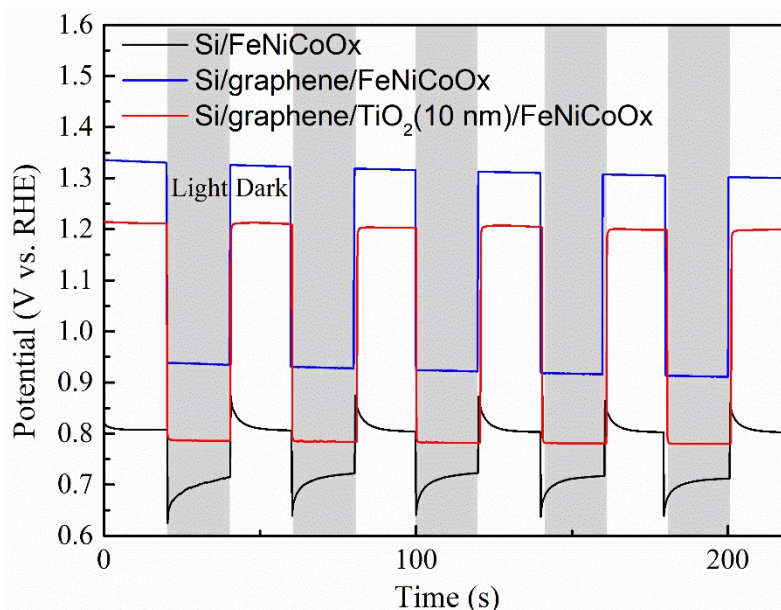
**Figure S7.** (a) Cyclic voltammograms (CVs) of FeNiCoO<sub>x</sub>, FeNiO<sub>x</sub> and FeCoO<sub>x</sub> films. (b) Tafel plots obtained for these films. (c) Current density *versus* applied voltage, without and with *iR* drop correction (plain and dash lines respectively) for the FeNiCoO<sub>x</sub>, FeNiO<sub>x</sub> and FeCoO<sub>x</sub> films. (d) Transmittance of the as prepared FeNiCoO<sub>x</sub> film and the film after operation at different potentials. (e) CVs of FeNiCoO<sub>x</sub> films prepared with different annealing time. (f) CVs of FeNiCoO<sub>x</sub> films prepared with different concentration. The thickness of the film increased with the increase in the total metal complex concentration

Table S1. Overpotentials of the FeNiCoO<sub>x</sub>, FeNiO<sub>x</sub> and FeCoO<sub>x</sub> electrocatalysts.

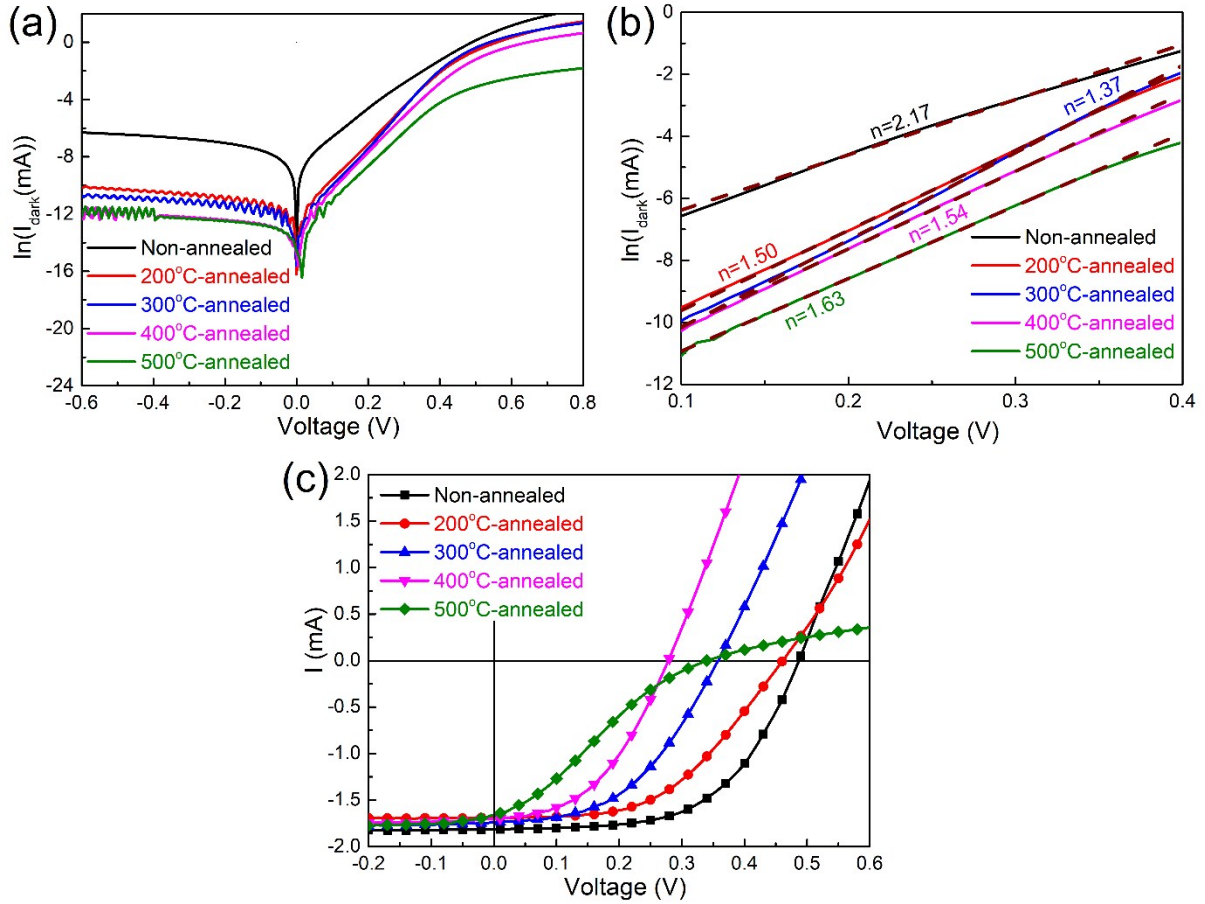
	FTO/FeNiCoO <sub>x</sub> (7.5%, 100 °C)	FTO/FeNiO <sub>x</sub> (7.5%, 100 °C)	FTO/FeCoO <sub>x</sub> (7.5%, 100 °C)	FTO/FeNiCoO <sub>x</sub> (7.5%, 150 °C)	FTO/FeNiCoO <sub>x</sub> (7.5%, 200 °C)
Overpotential (mV) at 10 mA/cm <sup>2</sup>	290±3	291±2	340±4	295±2	301±3

Table S2. Thickness, overpotential and transmittance of the FeNiCoO<sub>x</sub> film prepared with different total metal complex concentration and annealed at 100°C.

	Thickness (nm)	Overpotential (mV) at 10 mA/cm <sup>2</sup>	Transmittance (%) at 800 nm (1.5 V vs. RHE)
FTO/FeNiCoO <sub>x</sub> (3%)	200±12	310±5	95.3±1.8
FTO/FeNiCoO <sub>x</sub> (7.5%)	450±18	290±3	86.2±2.6
FTO/FeNiCoO <sub>x</sub> (15%)	870±26	289±2	63.5±4.1



**Figure S8.** Open circuit voltage (OCV) measurement of Si/FeNiCoO<sub>x</sub>, Si/graphene/FeNiCoO<sub>x</sub> and Si/graphene/TiO<sub>2</sub>(10 nm)/FeNiCoO<sub>x</sub> photoanodes. The change of OCP in the dark and under illumination corresponding to the photovoltage of the photoanodes.



**Figure S9.** Current-voltage curves of non-annealed and annealed Si/graphene micro-net samples (a) in the dark and (c) under AM 1.5G illumination ( $100 \text{ mW/cm}^2$ ). (b) is the diode ideality factor ( $n$ ). The annealing of the Si/graphene samples were conducted in pure Ar ambient at  $200 \text{ }^\circ\text{C}$  to  $500 \text{ }^\circ\text{C}$  for 30 min. The diode ideality factor ( $n$ ) presented in b is determined from the slope of the linear region of the forward-bias  $\ln(I_{\text{dark}})-V$  characteristics

through the relation:  $n = \frac{q}{kT} \left( \frac{dV}{d(\ln I_{\text{dark}})} \right)$ .  $n$  is the ideality factor that should be 1 if the

Schottky junction current is purely from thermionic emission. For non-annealed Si/graphene micro-net devices, the diode ideality factor is greater than 2. The diode ideality factors decrease to 1.50 and 1.37 for the annealing temperature of 200 and 300  $^\circ\text{C}$ , respectively. When the annealing temperature increase further, the ideality factors increase again. The results suggest that the diode effect of devices with a mild temperature annealing (200  $^\circ\text{C}$  to 300  $^\circ\text{C}$ ) becomes more desirable. However, annealing lead to a decreasing of the open-circuit voltage ( $V_{OC}$ ), so annealing temperature of 200  $^\circ\text{C}$  could maintain a high  $V_{OC}$  and a low  $n$ . Thus, we choose a deposition temperature of 200  $^\circ\text{C}$  during the  $\text{TiO}_2$  deposition process.

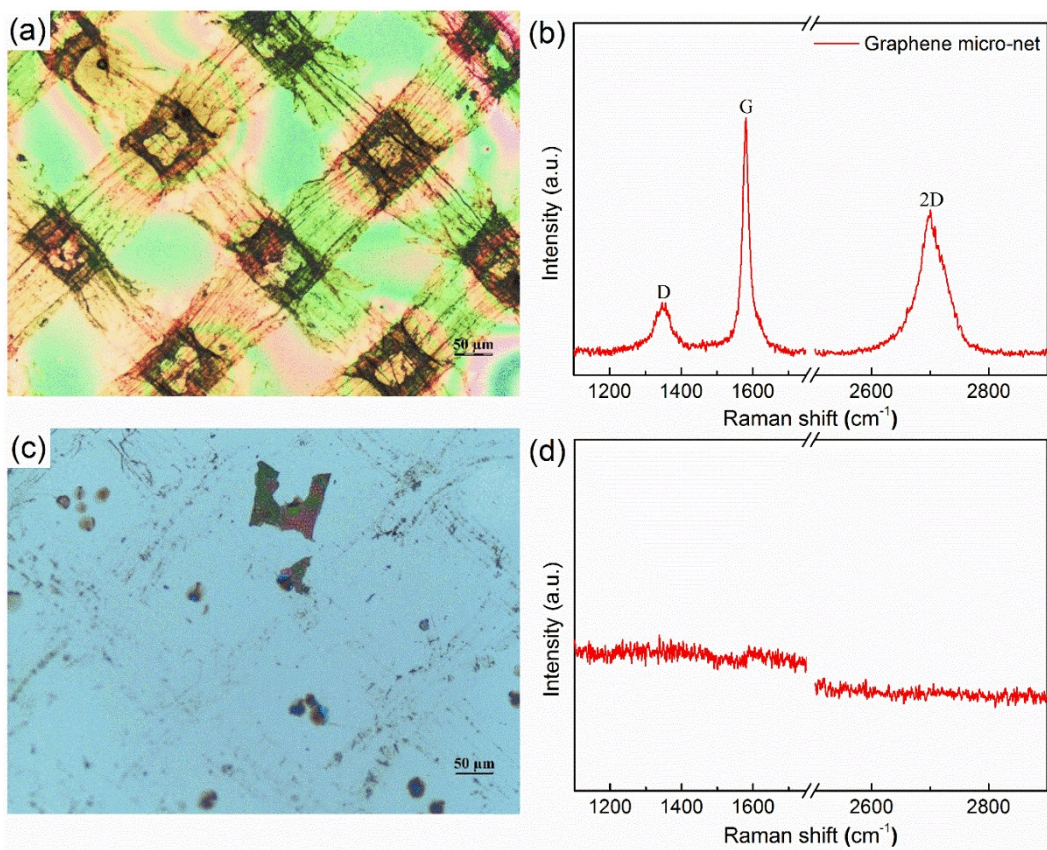


**Figure S10.** Microscopy images of the Si/graphene/FeNiCoO<sub>x</sub> photoanode (a) before and (c) after stability test. Raman spectra taken at the region with graphene (b) before and (d) after stability test.

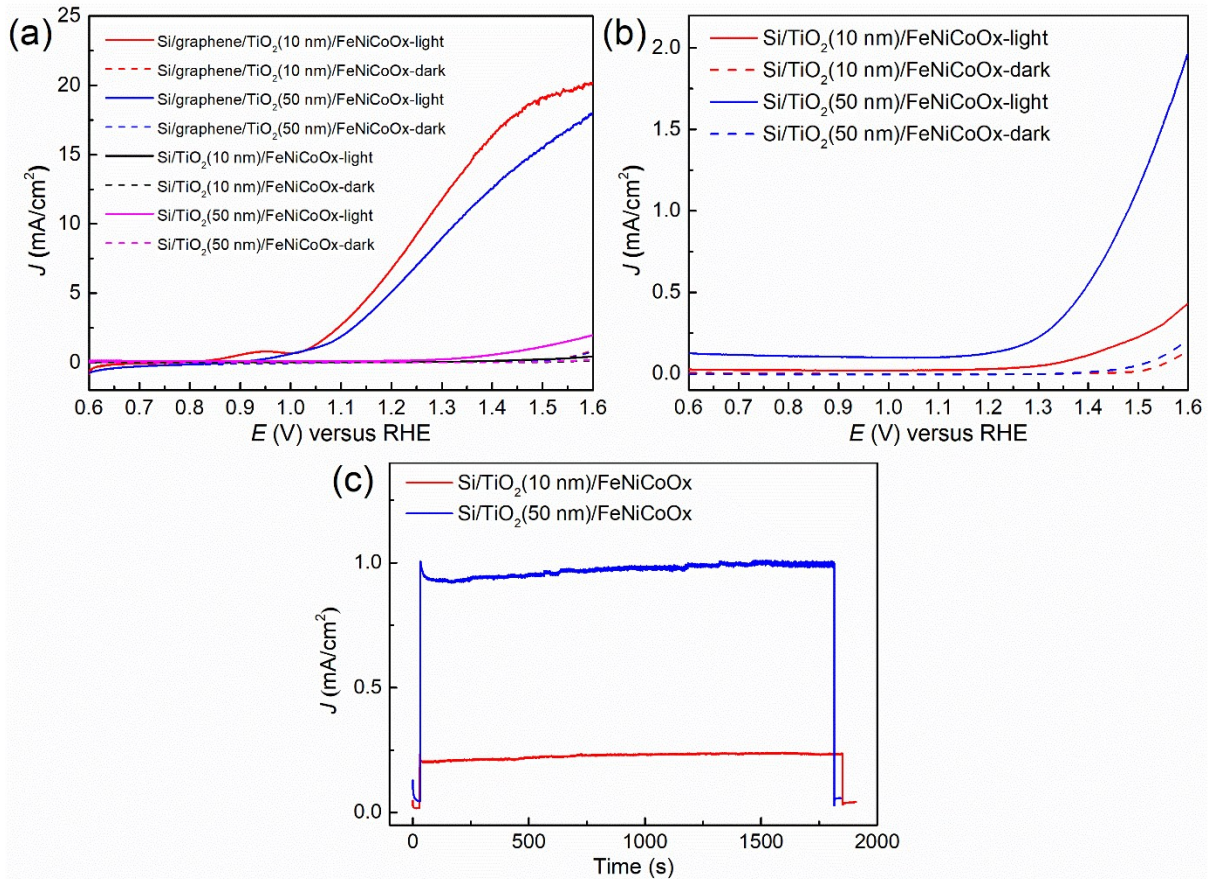


**Figure S11.** (a) Current-potential curves of Si/graphene/TiO<sub>2</sub> (10 nm)/FeNiCoO<sub>x</sub>, Si/graphene/TiO<sub>2</sub> (50 nm)/FeNiCoO<sub>x</sub>, Si/TiO<sub>2</sub> (10 nm)/FeNiCoO<sub>x</sub>, and Si/TiO<sub>2</sub> (50 nm)/FeNiCoO<sub>x</sub> photoanodes in 1 M NaOH under AM 1.5G light illumination (Scan rate: 10 mV/s). (b) Current-potential curves of Si/TiO<sub>2</sub> (10, 50 nm)/FeNiCoO<sub>x</sub> photoanodes in 1 M NaOH under AM 1.5G light illumination. (c) Stability test of Si/TiO<sub>2</sub> (10, 50 nm)/FeNiCoO<sub>x</sub> photoanodes at 1.5 V vs. RHE.

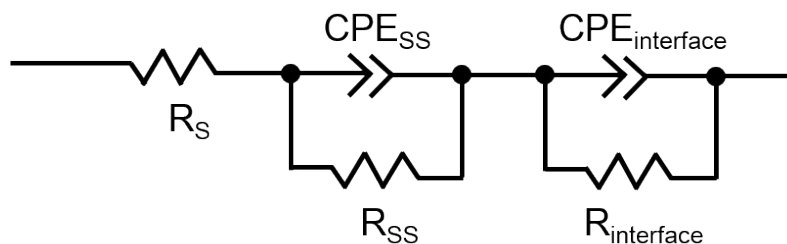


**Figure S12.** The equivalent circuit used for the Nyquist plots of the Si-based photoanodes. The two semi-circles observed in the EIS spectra are ascribed to the solid/solid junction of the Si/graphene and the interface junction of the TiO<sub>2</sub>/catalyst and/or TiO<sub>2</sub>/electrolyte [S1,S2]. The charge transfer resistance at the interface junction of the Si/graphene/TiO<sub>2</sub>/FeNiCoO<sub>x</sub> photoelectrode was measured to be  $\sim 330 \Omega$ , which is much smaller than that of the Si/FeNiCoO<sub>x</sub> photoelectrode ( $\sim 1700 \Omega$ ). The photoelectrode with a favorable Schottky junction can effectively enhance charge transfer from electrode surface to electrolyte.

**Table S3.** Fitting results obtained from EIS data of Figure 4(d).

	$R_s(\Omega)$	$R_{ss}(\Omega)$	$R_{interface}(\Omega)$	$CPE_{ss}(F)$	$CPE_{interface}(F)$
Si/FeNiCoO <sub>x</sub>	17.6	33000.6	1700.4	3.5E-5	4.1E-6
Si/graphene/FeNiCoO <sub>x</sub>	30.1	160.5	400.5	9.4E-5	6.5E-6
Si/graphene/TiO <sub>2</sub> (10nm)/FeNiCoO <sub>x</sub>	53.9	211.5	330.2	3.8E-6	4.3E-6

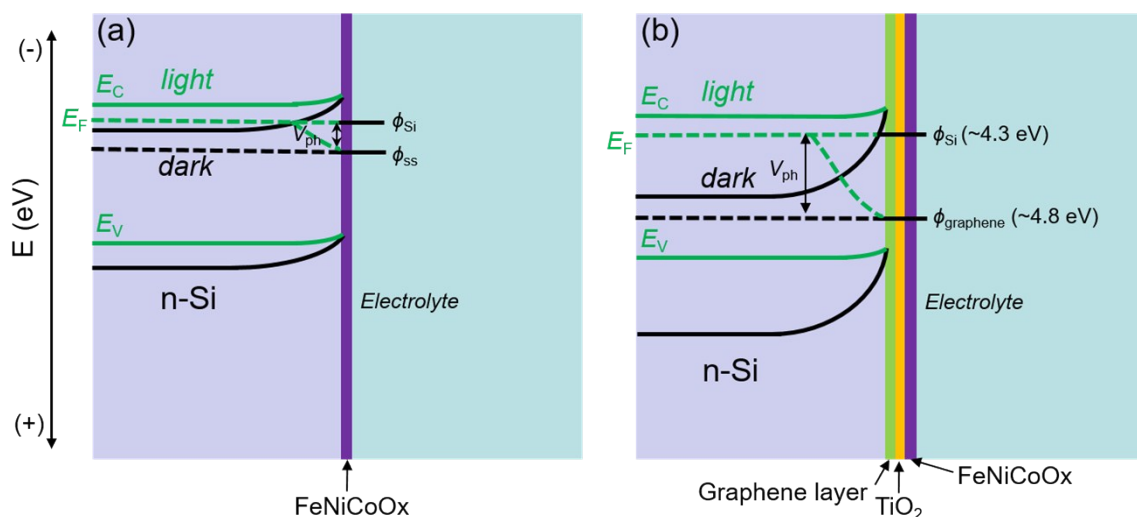


**Figure 13.** Structure of (a) Si/FeNiCoO<sub>x</sub> and (b) Si/graphene/TiO<sub>2</sub>/FeNiCoO<sub>x</sub> photoanodes and proposed energy band diagram in the dark (dark) and under light illumination (green). The band edges are assumed to be pinned at the solid/liquid interface. For the Si/FeNiCoO<sub>x</sub> structure, due to the permeable co-catalyst film and nonideality factors representing effects such as the surface states on Si surface, the built-in potential of Si/electrolyte solid/liquid junction is determined by the difference between the work function of Si ( $\phi_{Si}$ , ~4.3 eV) and the surface state energy level ( $\phi_{ss}$ ). [S3] Therefore, a small band bending in Si was formed, which accounted for the low photovoltage (~100 mV). By introducing a graphene layer on Si, the barrier height of Si/graphene Schottky barrier is mainly defined by the difference between the work functions of Si ( $\phi_{Si}$ , ~4.3 eV) and graphene layer ( $\phi_{graphene}$ , ~4.8 eV) [S4] and thus the barrier height providing a large driving force for the PEC oxygen evolution. In this study, the higher photovoltage of ~420 mV observed on the photoanode with Si/graphene heterojunction indicates that an efficient solid/solid junction was formed. The high built-in field across the interface is favorable to the charge separation and transfer toward the Co-catalyst/electrolyte interface.

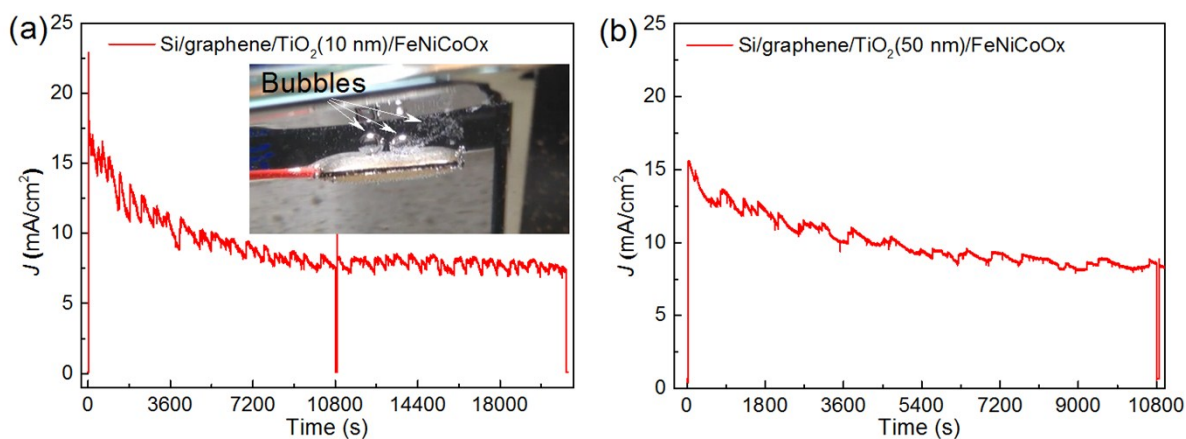


**Figure S14.** Current–time curves (held at 1.5 V vs. RHE) of Si/graphene/TiO<sub>2</sub>/FeNiCoO<sub>x</sub> photoanodes with different TiO<sub>2</sub> thickness: (a) 10 nm; (b) 50 nm.

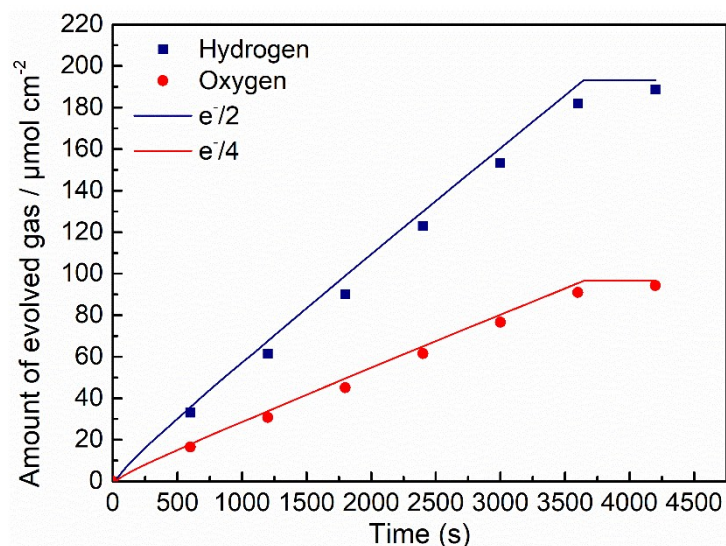


**Figure S15.** The plots for the amounts of the evolved gases (H<sub>2</sub> and O<sub>2</sub>) for Si/graphene/TiO<sub>2</sub>(10 nm)/FeNiCoO<sub>x</sub> recorded at 1.5 vs. RHE under illumination of 50 mW/cm<sup>2</sup> (100 W xenon lamp). A 1 M NaOH was used as an electrolyte. The blue and red lines in indicate the expected gas amounts of H<sub>2</sub> and O<sub>2</sub>, respectively, calculated from the total charge recorded as the photocurrent.

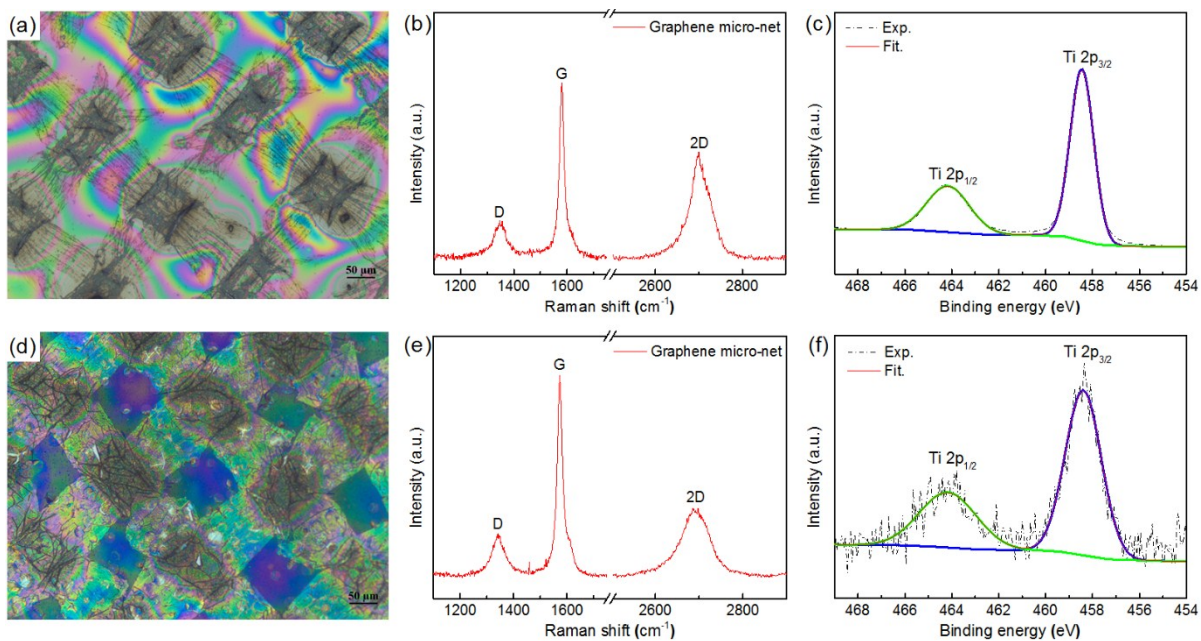


**Figure S16.** Microscopy images of the Si/graphene/TiO<sub>2</sub>/FeNiCoO<sub>x</sub> photoanode (a) before and (d) after stability test. Raman spectra taken at the region with graphene (b) before and (e) after stability test. (c) XPS spectrum of Ti-2p peak of Si/graphene/TiO<sub>2</sub> sample. (f) XPS spectrum of Ti-2p peak of Si/graphene/TiO<sub>2</sub>/FeNiCoO<sub>x</sub> sample after stability test.

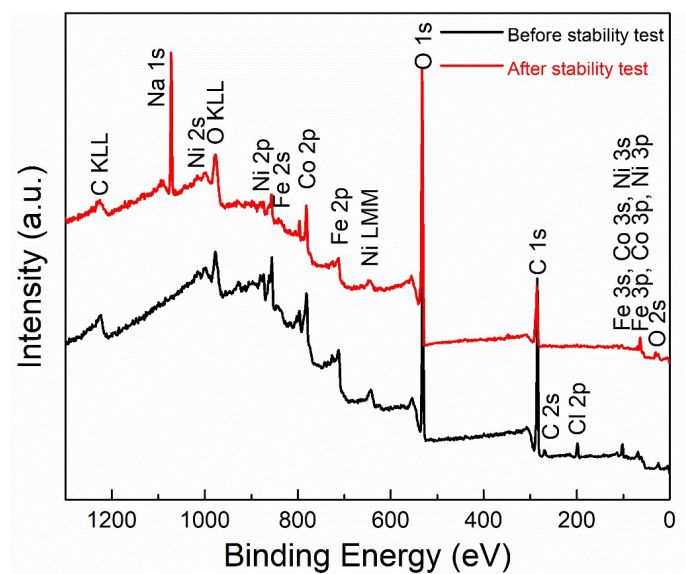


**Figure S17.** X-ray photoelectron spectroscopy survey scan acquired on Si/graphene/TiO<sub>2</sub> (10 nm)/FeNiCoO<sub>x</sub> before and after stability test.

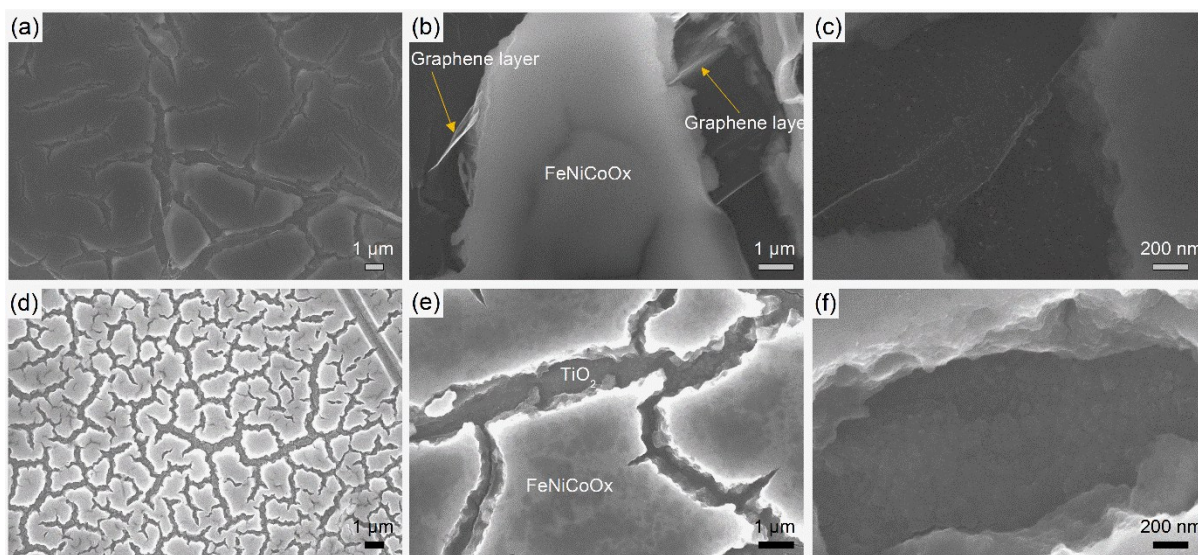


**Figure S18.** (a-c) FE-SEM images of the Si/graphene/TiO<sub>2</sub> (10 nm)/FeNiCoO<sub>x</sub> photoanode after 3h stability test. (d-f) FE-SEM images of the Si/graphene/TiO<sub>2</sub> (50 nm)/FeNiCoO<sub>x</sub> photoanode after 3h stability test.

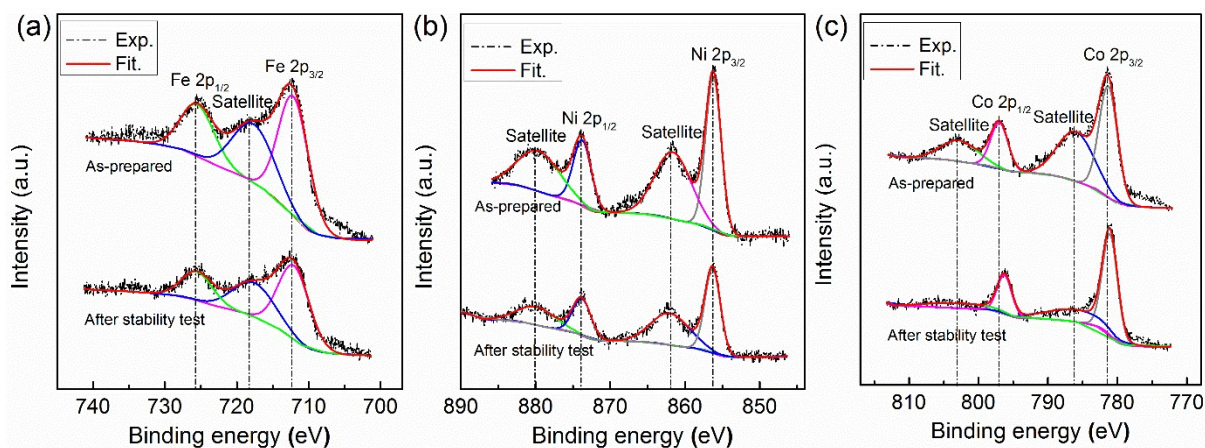


**Figure S19.** High resolution XPS spectra of (a) Fe-2p, (b) Ni-2p and (c) Co-2p peaks of the FeNiCoO<sub>x</sub> film on Si/graphene/TiO<sub>2</sub> electrode before and after stability test.

### References:

- [S1] Yu, X.; Yang, P.; Chen, S.; Zhang, M.; Shi, G. NiFe Alloy Protected Silicon Photoanode for Efficient Water Splitting. *Adv. Energy Mater.* **2017**, *7*, 1601805.
- [S2] Zhong, M.; Hisatomi, T.; Kuang, Y.; Zhao, J.; Liu, M.; Iwase, A.; Jia, Q. M.; Nishiyama, H.; Minegishi, T.; Nakabayashi, M.; Shibata, N.; Niishiro, R.; Katayama, C.; Shibano, H.; Katayama, M.; Kudo, A.; Yamada, T.; Domen, K. Surface Modification of CoO<sub>x</sub> Loaded BiVO<sub>4</sub> Photoanodes with Ultrathin p-Type NiO Layers for Improved Solar Water Oxidation. *J. Am. Chem. Soc.* **2015**, *137*, 5053.
- [S3] Digdaya, I. A.; Han, L.; Buijs, T. W.; F. Zeman, M.; Dam, B.; Smets A. H.; M. and Smith, W. A. *Energy Environ. Sci.*, **2015**, *8*, 1585-1593.
- [S4] X. Li, P. Sun, L. Fan, M. Zhu, K. Wang, M. Zhong, J. Wei, D. Wu, Y. Cheng and H. Zhu, *Sci. Rep.*, **2012**, *2*, 395.